W.-L. Huang, Z. Ren, and C. T.-C. Nguyen, "Nickel vibrating micromechanical disk resonator with solid dielectric capacitive-transducer gap," *Proceedings*, 2006 IEEE Int. Frequency Control Symp., Miami, Florida, June 5-7, 2006, pp. 839-847.

Nickel Vibrating Micromechanical Disk Resonator With Solid Dielectric Capacitive-Transducer Gap

Wen-Lung Huang, Zeying Ren, and Clark T.-C. Nguyen
Center for Wireless Integrated Micro Systems
Department of Electrical Engineering and Computer Science
University of Michigan, Ann Arbor, Michigan 48109-2122, USA

***Abstract*—A MEMS-based vibrating disk resonator fabricated in a low temperature nickel metal material and using a 30-nm nitride dielectric capacitive transducer has been demonstrated at frequencies approaching 60 MHz with *Q*'s as high as 54,507, which is the highest to date for any *micro*-scale *metal* resonator in the VHF range. The frequency-*Q* product of 3.3×10^{12} achieved by this device is three orders of magnitude higher than the 1.1×10^{9} of previous *nickel* micromechanical resonators. The degree of isolation afforded by its supports strongly governs the achievable *Q*'s of this device, which vary from 490 when a 2 μm-radius supporting stem is used, to 54,507 when no stem is used, clearly indicating an anchor dominated loss mechanism, but more importantly indicating that nickel's intrinsic material *Q* is quite high at VHF. Furthermore, because its highest process temperature is 380°C, and there are paths to an even lower temperature ceiling (e.g., 100°C), the fabrication process for nickel disks is amenable to post-processing over finished foundry CMOS wafers, even those using advanced low-k dielectrics around copper metallization. Nickel material thus presents an intriguing path towards a complete communication transceiver (including all high *Q* passives) on a chip.**

***Keywords*—MEMS, micromechanical resonator, nickel, capacitive transducer, quality factor, charge bias, integration.**

I. Introduction

The advent of vibrating micromechanical resonators operating at GHz frequencies with *Q*'s >10,000 [1][2][3] has generated great interest in RF front-end architectures that dispense with previous restrictions on the number of high *Q* passives used, and rather attempt to utilize them in massive quantities in order to achieve enhanced robustness, lower power consumption, and greater multi-mode reconfigurability [4]. Among the more aggressive of the proposed architectures that fully harness the capabilities of vibrating RF MEMS is one based on a front-end RF channel-selector, where micromechanical filters [5] placed in large banks directly after the antenna can be switched on and off to select the desired channel(s) directly at RF. Hundreds, perhaps thousands, of filters might be required to cover all needed bands in a practical implementation, but if MEMS technology can truly realize the dense integrated micromechanical circuits predicted and described in [6], then such numbers would not be problematic.

Interconnecting the many elements of such an integrated micromechanical circuit to transistor electronic circuits, however, poses a challenging prospect. In particular, the number and density of interconnections to the many micromechanical filters might make a bond-wire approach impractical, or uneconomical. When the number of required MEMS-to-transistor interconnects exceeds 1000, direct monolithic integration of MEMS and transistors onto a single die becomes a much more attractive approach to interconnection.

To date, several approaches to monolithic integration of MEMS and transistors have been developed and implemented over the past decade. The most prevalent methods in production [7] presently utilize process flows that intermix and share steps from the original stand-alone MEMS and transistor process flows, seeking to reduce the total number of steps required in a given merging process. Unfortunately, however, such an intermixed process often precludes advancement in the base MEMS or transistor technologies used, since altering one of the base processes would require a redesign of the whole integration process. It is for this reason that many products based on intermixed integration processes still use 1980's transistor circuit technology; i.e., switching to a more modern transistor technology (e.g., with 65 nm channel lengths) would be too costly.

To allow process advancement in next generation products, more modular approaches to integration have been developed that separate the base MEMS and transistor process flows into modules and run one module before the other, with no intermixing of steps. In such a process, a change in one module could ideally be made without affecting the other module or the method of modular merging. Advancements in a particular module could be incorporated without a redesign of the whole process. To date, several modular MEMS-transistor merging processes have been demonstrated, some placing the MEMS module before the transistor one [8][9], others vice versa [10][11][12]. Of these processes, the ones based on post-transistor MEMS are perhaps most amenable to integration with foundry CMOS. In particular, pre-transistor MEMS processes require that IC foundries accept wafers that have been pre-processed, and so far, IC foundries have been reluctant to do this.

The MICS process [11][12], summarized very briefly in Fig. 1, integrates MEMS directly over CMOS in a fully

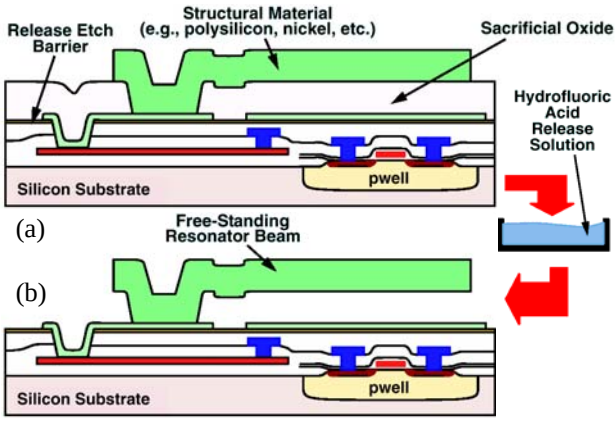

Fig. 1: Cross-sections (a) immediately before and (b) after release in the original polysilicon MICS process, a surface-micromachining process done directly over CMOS [11].

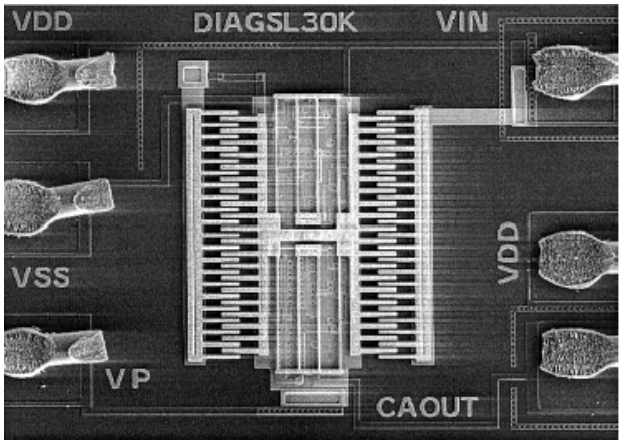

Fig. 2: SEM of a poly$Si_{0.35}Ge_{0.65}$ resonator fabricated atop a CMOS amplifier with Al-Si(2%) interconnect using the MICS process [12].

planar process. Originally done using polysilicon MEMS, the latest rendition of MICS, shown in Fig. 2, uses poly-SiGe MEMS above 0.18 μm CMOS and is presently among the most successful pre-transistor processes available. The key to this process is the ability to deposit poly-SiGe MEMS structural material at temperatures below 450°C, which can be withstood by copper metallization and associated dielectrics used in 0.18 μm CMOS processes. Next generation CMOS processes, however, from 65 nm on down, are beginning to use low-k dielectric materials over their metals that may no longer survive temperatures over 400°C. To accommodate this lower temperature ceiling, new structural materials are needed for vibrating RF MEMS applications that can be deposited at very low temperatures while still retaining high *Q*. It is possible that a temperature ceiling as low as 200°C might eventually be needed as transistor technology continues to advance.

Pursuant to finding such a material, this work investigates nickel as a potential high frequency, high *Q* structural material for RF applications. In particular, a MEMS-based vibrating disk resonator fabricated in a low temperature nickel metal material and using a 30 nm nitride dielectric capacitive transducer has been demonstrated at frequencies around 60 MHz with *Q*'s as high as 54,507, which is the highest to date for any *micro*-scale *metal* resonator in the VHF range. The frequency-*Q* product of 3.3×10^{12} achieved by this device is three orders of magnitude higher than the 1.1×10^{9} of previous *nickel* micromechanical resonators. Because its highest process temperature is 380°C, and there are paths to an even lower temperature ceiling (e.g., 100°C), the fabrication process for this nickel disk is amenable to post-processing over finished foundry CMOS wafers, even those using advanced low-k dielectrics around copper metallization. The nickel material of this work thus presents a potential path towards a complete communication transceiver (including all high *Q* passives) on a chip.

II. Intrinsic Loss or Anchor Loss?

With an electroplating deposition temperature of only 50°C, nickel was recognized early as a potential structural material for post-transistor high *Q* vibrating RF MEMS devices. Most notable among efforts to use nickel as a resonator structural material is the ring gyroscope by Putty and Najafi [10] in 1994, which not only achieved a functional gyroscope, but also integrated the micromechanical resonating proof mass element together with active CMOS electronics, all in a single planar process that realized the MEMS in post-transistor fashion. Although the gyroscope was functional, the *Q* of its 33.5-kHz plated-nickel proof mass resonator was only 2,400, and its frequency drifted at a rate of 14ppm/day. These problems compelled researchers to abandon nickel as the structural material and replace it with single-crystal silicon, which was more stable and capable of much higher *Q*'s. With a resolution 7.2°/hr, the single-crystal silicon vibratory ring gyroscope of [13] is still among the lowest resolution MEMS-based gyroscopes implemented to date.

Despite the *Q* and drift problems encountered in early attempts to use nickel structural material in MEMS devices, efforts to improve the material continued, spurred by its great potential for post-transistor planar integration. In 1999, work by Hsu and Nguyen [14] introduced a method dubbed "in situ localized annealing", where an electrical current is sent through the conductive mechanical structure of a resonator device to heat it to temperatures as high as 886°C while vibrating the device at its resonance frequency. Application of this method to 75-kHz folded-beam resonators was found to raise their *Q*'s from 4,103 to 14,172, and to greatly improve their drift stability. In principle, operation of the resonator device at high temperature is thought to redistribute or remove defects and contaminants from its volume and surfaces, effectively removing intrinsic loss mechanisms, and thereby allowing much higher *Q* and stability.

Later attempts in 1999 to apply localized annealing to higher frequency clamped-clamped beam ("CC-beam") and free-free beam ("FF-beam") resonators made in nickel structural material, however, were not successful. In par-

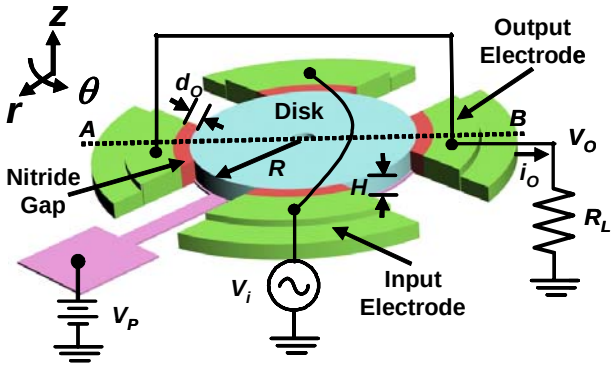

Fig. 3: Perspective view schematic of a solid dielectric gap disk resonator identifying key features and showing a two-port measurement scheme.

ticular, only CC-beam devices were functional in the only fabrication run devoted to this evaluation, and these posted *Q*'s on the order of only 532. The FF-beam devices, which were much better isolated from their anchors, were unfortunately not functional. Thus, at the time this work was discontinued shortly after 2000, there was no conclusion on whether the low *Q*'s of VHF CC-beam nickel resonators were caused by anchor loss mechanisms, or intrinsic material loss mechanisms.

III. Resonator Types Under Test

To quantify the influence of anchor losses on nickel resonator *Q*, this work focuses on the compound (2,1) mode disks, often dubbed "wine-glass disks", first introduced in [15]. This wine-glass disk design is quite suitable for anchor loss evaluation, since, as shown in [15], the amount of anchor loss experienced by this particular design can be specified by selection of the anchor type (i.e., center stem or side support), the number of anchors, and the geometry of the anchors (i.e., stem size).

Figure 3 presents the perspective-view schematic of one of the wine-glass disk resonators used in this work, hooked up in its typical electrical bias, excitation, and measurement scheme. As seen in the figure, the device is composed of a 3 μm-thick nickel disk resonator suspended 400 nm above a ground plane by a stem placed at the disk center and anchored to the substrate below. Four separate electrodes spaced less than 100 nm from the disk edges are placed on four different quadrants surrounding the disk to specifically excite its compound (2,1) mode, which is shown in Fig. 4. In practice, the gaps between the resonator and its electrodes can be either air-filled or solid-filled, with the latter the more preferable, since solid-filled gaps both reduce resonator impedance and raise the fabrication yield of devices.

To operate this device, a DC bias V_P is applied to the disk structure and an AC input voltage v_i is applied to one pair of opposing electrodes along the same axis (i.e., the input axis). (Note that no current flows once the structure is charged to V_P, so there is no dc power consumption.) These voltages then collectively create a time-varying electrostatic excitation force between the electrodes and the disk, in the lateral

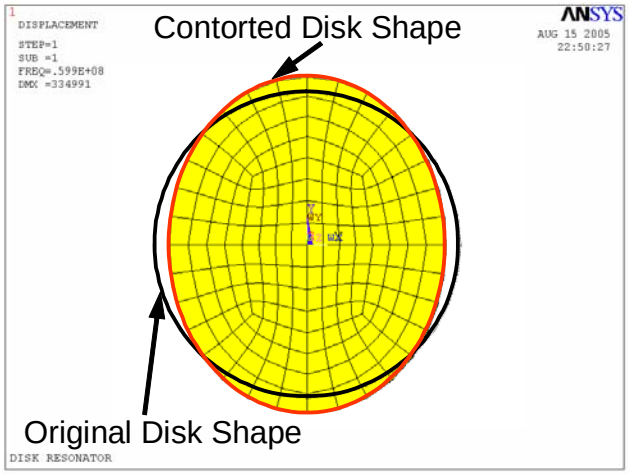

Fig. 4: Vibration mode shape for an 18 μm radius wineglass mode disk micromechanical resonator obtained via ANSYS FEA.

direction, and at the frequency of the AC input voltage if $V_P > v_i$. When the AC input frequency matches the disk resonance frequency, the resulting resonance electrostatic force drives the disk into resonance vibration, which then generates resonance motion along the orthogonal output axis, depicted in Fig. 3. Motion along the output axis results in a DC biased time-varying capacitance at the output electrodes, which produces an output current i_o given by

$$i_o = V_P\left(\frac{\partial C}{\partial t}\right) \cong V_P \cdot \left(\frac{\varepsilon_o A_o}{d_o^{\,2}}\right) \cdot \omega_o X = \frac{\omega_o Q V_P^{\,2}}{k_r} \cdot \frac{\varepsilon_o^{\,4} \pi^2 R^2 H^2}{d_o^{\,4}} \cdot v_i \qquad (1)$$

where $A_o = (\pi R)H$, R, H, d_o, k_r and Q are the electrode-to-resonator overlap area, radius, thickness, gap spacing, effective stiffness, and quality factor, respectively, of the disk resonator; X is the amplitude of resonator vibration; $\omega_o = 2\pi f_o$ is the radian resonance frequency; ε_o is the dielectric constant; and an approximate form for $\partial C/\partial t$ has been used.

The expression for resonance frequency has been presented previously in [16], but is repeated here for convenience, as

$$\left[\Psi_2\left(\frac{\varsigma}{\xi}\right) - 2 - q\right] \cdot \left[\Psi_2(\varsigma) - 2 - q\right] = (2q-2)^2 \qquad (2)$$

where

$$\Psi_2(x) = \frac{xJ_1(x)}{J_2(x)}$$
$$q = \frac{\varsigma^2}{2n^2 - 2}$$
$$\varsigma = 2\pi f_0 R\sqrt{\frac{\rho(2+2\sigma)}{E}} \qquad (3)$$
$$\xi = \sqrt{\frac{2}{1-\sigma}}$$

and where $J_n(x)$ is the Bessel function of first kind of order n, f_o is the resonance frequency, and ρ, σ and E, are the density, Poisson ratio, and Young's modulus, respectively, of the disk structural material.

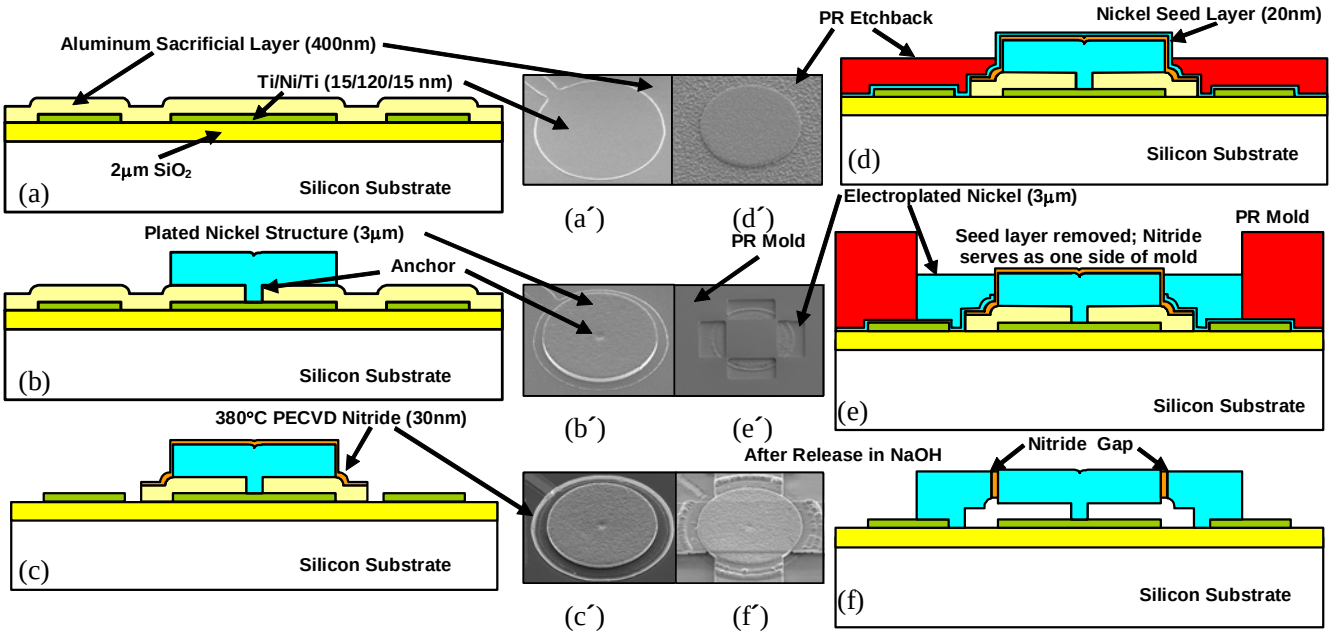

Fig. 5: Cross sectional fabrication process flow and associated SEM's for laterally vibrating nickel disk resonators with solid dielectric gap.

IV. Nickel Disk Fabrication Process

The fabrication process used for the solid-dielectric gap nickel resonators of this work is presented in Fig. 5, which shows cross-sections and associated scanning electron micrographs (SEM's), taken along the AB plane of Fig. 3. The process begins with the wet oxidation growth of a 2 μm layer of oxide to provide electrical isolation between the conductive silicon substrate and the eventual nickel resonators and interconnects. 15 nm/120 nm/15 nm-thick Ti/Ni/Ti metal interconnects are then evaporated and patterned via lift-off, then buried under 400 nm of evaporated aluminum to achieve the cross-section shown in Fig. 5(a). The aluminum serves as a sacrificial layer to be removed later in the process. After wet etching anchor vias into the sacrificial aluminum using a solution of $H_3PO_4/HNO_3/H_2O$, 20 nm of nickel is evaporated over the entire wafer to serve as a seed layer for subsequent nickel plating. 3 μm of nickel structural material is then electroplated in a 50°C solution of nickel sulfate through a photoresist mold defining the disk structure. The mold and seed layer are then stripped using a PRS-2000 solution and a custom-made $CH_3COOH/HNO_3/H_2SO_4/H_2O$ nickel etchant solution [17], respectively, to achieve the cross section of Fig. 5(b).

At this point, the disk structure is fully formed. It should be noted that the etch time in the seed-removing nickel etchant should be minimized, since this etchant also attacks the structural material, and will degrade the *Q* and stability of eventual μresonators if allowed to etch for lengthy periods. Regarding the 3 μm thickness of the disk, it should be noted that much thicker nickel films are possible via electroplating. In particular, films up to 1000 μm are possible using the

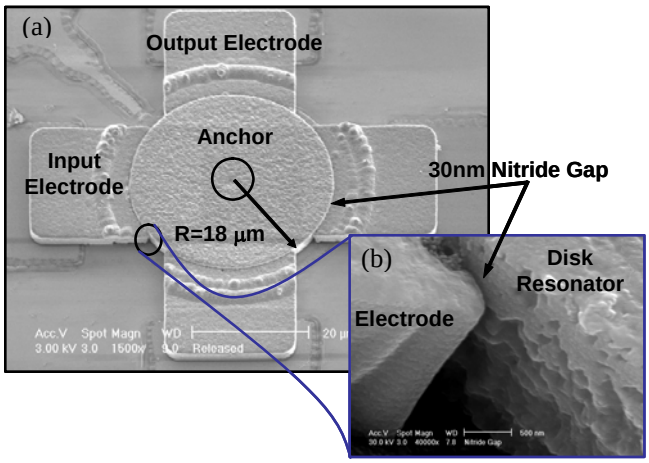

Fig. 6: (a) Wide-view and (b) gap-zoomed SEM's of a fabricated nickel disk resonator supported by a stem anchored at its center.

LIthographie Galvanik Abformung (LIGA) process [18].

After the disk structures have been formed and the photoresist molds removed, a 30 nm-thick film of PECVD silicon nitride is then deposited at 380°C conformally over all surfaces, including and especially over the disk sidewalls, where it serves as the electrode-to-resonator gap material. At present, this nitride deposition represents the highest temperature step in the process. If 380°C is too high, then other methods for growing conformal dielectric films are available, such as atomic layer deposition (ALD), which can grow thin dielectric films at temperatures as low as 100°C [19].

To prepare for electrode formation, a combination of dry and wet etches are first used to expose interconnects and bond pads, yielding the cross-section of Fig. 5(c). Electrode construction then starts with the evaporation of another

20 nm-thick film of nickel to serve as another seed layer, this time for eventual electrode electroplating. To prevent plating over the top of disk structure when electrodes are plated, the nickel seed layer material atop the disk must first be removed. Pursuant to this, 13 μm of AZ9260 photoresist is spun and etched back by an O_2-based reactive ion etch (RIE) to expose the seed layer atop the structure, yielding the cross-section shown in Fig. 5(d). The "top" seed layer is then removed by wet-etching using the solution of [17], leaving nickel seeding material still over the electrode regions. The photoresist is then stripped, and a new film of 6 μm thick AZ9260 photoresist is spun, exposed, and patterned, to form a mold defining one side of the electrodes. (The other side is defined by the nitride-encapsulated disk edges.) Nickel is again electroplated 3 μm-thick to achieve the cross-section of Fig. 5(e). Finally, the structure is released in 50°C sodium hydroxide solution, which provides high aluminum-to-nickel and aluminum-to-nitride selectivity. The final cross section is shown in Fig. 5(f).

Although the process flow of Fig. 5 features a solid-dielectric gap between the resonator and electrode, the process can easily be transformed to yield air-gap devices by merely including a step to remove the dielectric gap film between the electrode and resonator. In this case, the process would be simpler if the gap material were oxide instead of nitride, since then the gap could be cleared during the device release step.

Figure 6(a) presents the wide-view SEM of a fabricated and released nickel disk resonator with an 18 μm disk radius and 1.5 μm stem radius. The inset in (b) zooms in on the 30 nm nitride gap, revealing a problem with electrode formation during processing. In particular, rather than sitting flush against the disk sidewalls, the electrodes have been undercut near the device so that the actual electrode-to-resonator overlap is much smaller than intended. These imperfect electrodes effectively reduce the overall drive and sense electrode overlap area in fabricated devices, which then makes measurement of these resonators a bit more difficult than usual (but not impossible).

V. Experimental Results

Table I summarizes the nickel wine-glass mode disk resonator designs evaluated in this work. Disk devices designed to these specifications were fabricated using the process flow described in Section IV, then tested in a custom-built chamber that could be pumped down to pressures below 50 μTorr. Pressures this low were needed to eliminate the influence of viscous gas damping on the *Q*'s of the resonator devices [20], thereby eliminating gas damping as a mechanism for *Q*-limiting, and hence, better elucidating other loss mechanisms. For testing, each die containing many resonator devices was mounted on a printed circuit board that was then placed into the test chamber. Individual devices were accessed by bond wiring to metal traces on the board, and air-tight electrical feedthroughs into and out of the vacuum chamber provided both DC and coaxial electrical interconnections between the board and external measurement instrumentation.

Table I: Nickel Disk Resonator Design and Performance Summary

Parameter	Center Stem Radius, 2μm	Center Stem Radius, 1.5μm	Stemless	Units
Radius: *R*, Thickness: *H*	18, 3	18, 3	18, 3	μm
Electrode to Resonator Gap: d_o	30	30	30	nm
DC Bias Voltage: V_P	5	9	5	V
RF Input Amplitude: v_{RF}	3.56	3.56	1.59	V
LO Carrier Amplitude: v_{LO}	9.98	6.25	1.59	V
Measured Frequency: f_o	60.04	59.65	59.96	MHz
Quality Factor In Vacuum: *Q*	490	5,077	54,507	—

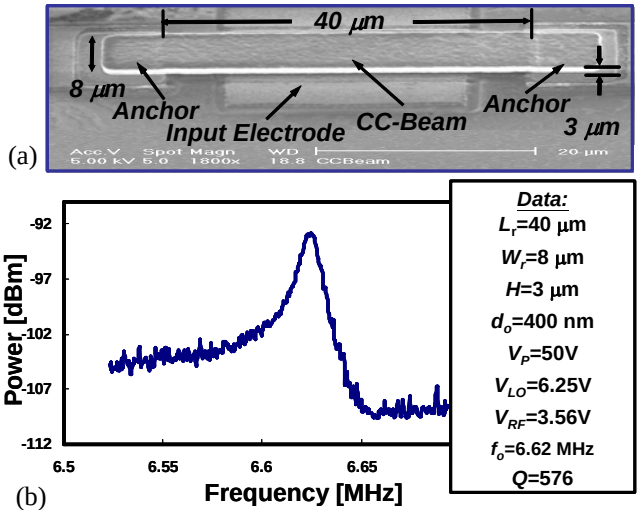

Fig. 7: (a) SEM and (b) measured frequency characteristic for a 6.6-MHz vertically actuated clamped-clamped beam resonator measured using the mixing measurement technique of [21].

A. Nickel CC-Beams

In addition to wine-glass disks, CC-beam resonators were also included in the process run in order to gauge the material quality of present fabrication run versus ones that had been run previously [14]. Figures 7(a) and 7(b) present the SEM and measured frequency characteristic, respectively, for a 40 μm-long, 8 μm-wide, 3 μm-thick vertically resonant CC-beam micromechanical nickel resonator achieved in this run. Because the 400 nm vertical electrode-to-resonator gap achieved by the present process (which is not optimized for vertical CC-beam resonators) is much smaller than the usual 100 nm used for such devices, this device has a much weaker capacitive transducer than previous CC-beams, so its motional output currents are substantially smaller. To isolate the

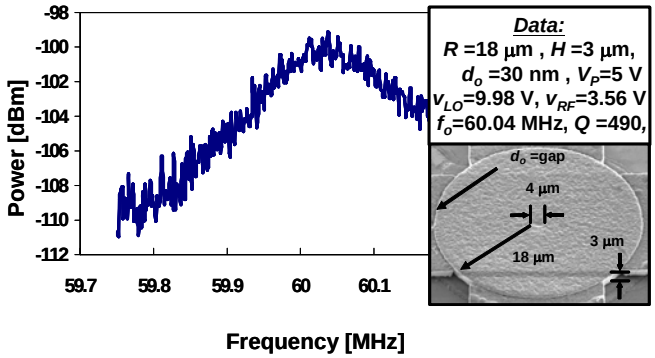

Fig. 8: Frequency characteristic of a 60-MHz wine-glass mode nickel disk supported by a 2 μm-radius center stem anchor measured using the mixing measurement technique of [21].

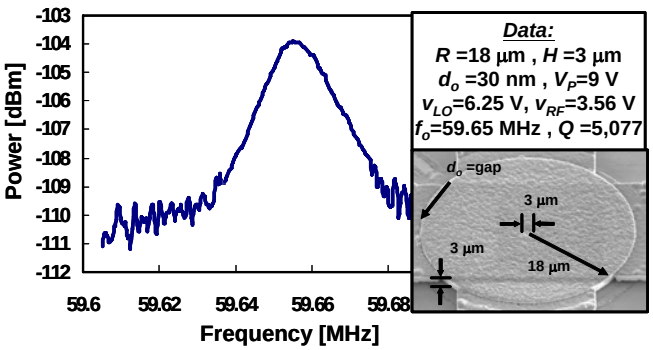

Fig. 9: Frequency characteristic of a 60-MHz wine-glass mode nickel disk supported by a 1.5 μm-radius center stem anchor measured using the mixing measurement technique of [21].

device's tiny motional current from feedthrough parasitic currents that might otherwise mask it, the mixing measurement scheme of [21] was used to detect and plot the device response, shown in Fig. 7(b). Because the mixing measurement method of [21] is used, the units of the y-axis of Fig. 7(b) are not dB's, but rather power dBm's, as measured by a spectrum analyzer in MAX HOLD mode [21]. In addition, the very low dBm levels seen in the data (and in data to follow) are caused by the impedance mismatch between the kΩ resonators and the 50Ω input of the spectrum analyzer, and are not indicative of actual device loss. The *Q* of the device gives a more accurate indication of its loss in a matched circuit application (e.g., in a filter).

From the measured response, the *Q* of this device is only 576 at 6.62 MHz. This is considerably lower than the 6,000-8,000 posted by previous 8.51-MHz polysilicon CC-beam resonators [22]. Without careful consideration, one might conclude from this result that nickel material has a lower intrinsic *Q* than polysilicon at HF to VHF frequencies. Such a conclusion, however, would only be valid if the anchor losses known to dominate the *Q*'s of polysilicon CC-beams were identical to those in the nickel ones. This might in fact not be the case, since there is evidence that the attachment of nickel resonators to the substrate at their anchors might not be as sturdy as their polysilicon counterparts. In particular, poor adhesion caused by the stress of the plated film between the structure and the substrate might result in a weak anchor that ultimately dissipates more energy during vibration. Thus, it is difficult to make any conclusions regarding loss mechanisms based on CC-beam measurements.

B. Nickel Wine-Glass Disks With Stems

The anchor loss uncertainties posed by the above CC-beam device are not shared by the wine-glass disk resonators of this work, since the latter possess support structures that better isolate the disks from their anchors. As described in [15] and [16], the amount of isolation achieved is a strong function of (1) the size of the supporting center stem; (2) whether or not a stem is even used; (3) the dimensions of any side supports; and (4) the number and placement of side supports used. Due to lithography issues during the fabrication run, the side-supported devices of this work were not testable, and only stem-supported devices were available for testing. In addition, due to the incomplete electrode-to-resonator overlap shown in Fig. 6, the mixing measurement scheme of [21] was again required for measurement of disk devices.

Since the anchor dissipation of previous stem-supported disk resonators was found to be a strong function of stem radius [23], insights into the impact of anchor losses on nickel resonator *Q* can be obtained by merely measuring devices with different stem radii. Pursuant to this, Figure 8 presents the measured frequency characteristic for an 18 μm-radius nickel wine-glass disk with a rather large 2 μm-radius center stem, showing a *Q* of only 490 at 60 MHz. This measurement was repeated over more than ten resonators with this stem size, with all devices exhibiting *Q*'s under 500. Assuming a nickel density equal to the bulk value of 8.9 kg/m^3, the 60 MHz frequency of this device implies a Young's modulus of 195 GPa and acoustic velocity of 4,678 m/s for the plated nickel material of this work.

Next, a 1.5 μm-radius center stem wine-glass disk resonator was tested. Figure 9 presents the measured frequency characteristic, which again shows resonance at 60 MHz, but this time with a *Q* in excess of 5,077. Clearly, the size of the center stem is a dominant factor governing the *Q* of a nickel wine-glass disk. If so, then the maximum *Q* of such a disk should ensue if the center stem can be eliminated. As mentioned, the side-supported devices, which were devoid of center stems, were not functional due to fabrication issues in this particular run; so stemless side-supported devices were not available.

C. Stemless Nickel Wine-Glass Disks

Fortunately, there were devices on this run that had neither stems, nor side supports. These devices were designed to be supported only by the solid material in their electrode-to-resonator gaps. Such a device, however, poses some measurement difficulty, since it does not have a lead with which to apply a dc-bias V_P to its conductive disk structure.

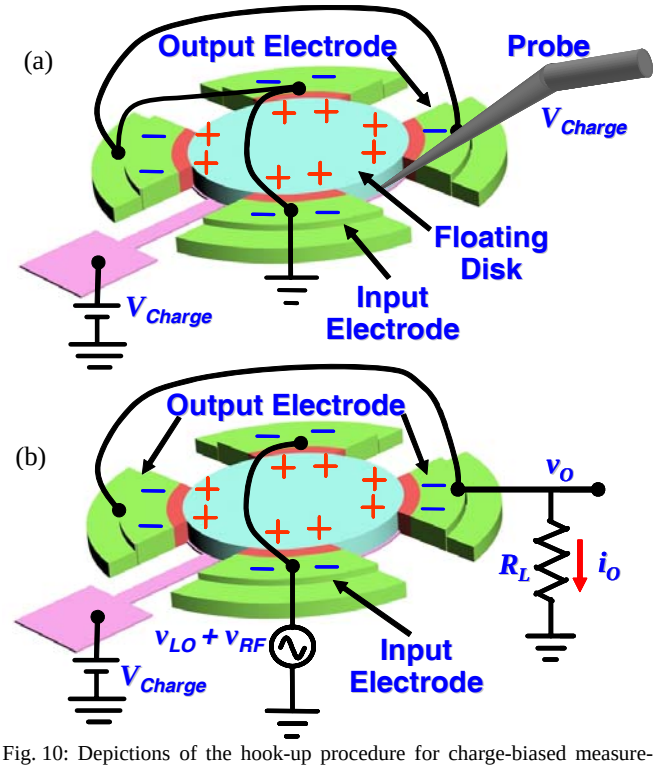

Fig. 10: Depictions of the hook-up procedure for charge-biased measurement. (a) Charge-biasing the disk structure via a charged probe tip. (b) Electrical hook-up for mixing measurement of a charge-biased resonator.

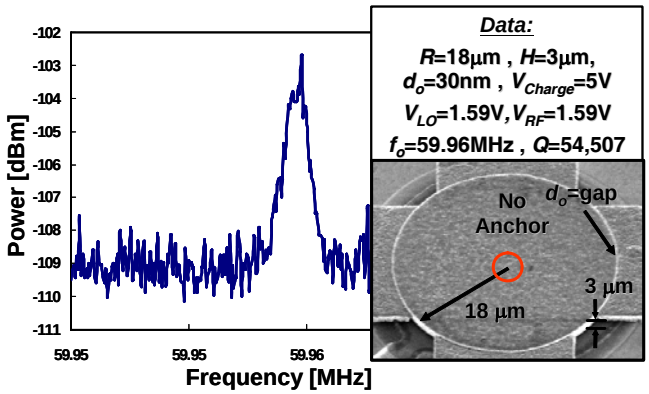

Fig. 11: Frequency characteristic of a stemless charge-biased 60-MHz wine-glass mode nickel disk measured via the mixing measurement technique of [21].

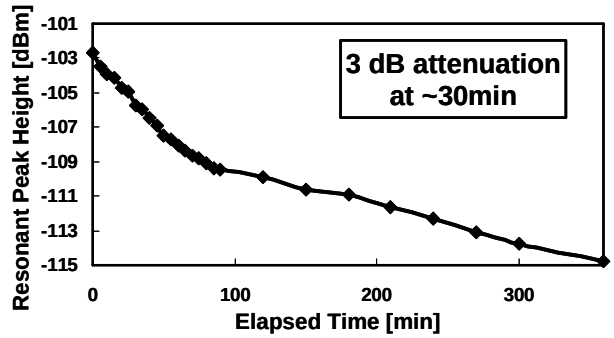

Fig. 12: Plot of resonance output amplitude versus discharging time for a charged-biased micromechanical nickel disk resonator.

Fortunately, such a lead is not needed, since charge biasing can be used [24], where charge is deposited onto the resonator structure using a probe. From [24], the discharge time for a charge-biased resonator can be quite long, on the order of 900s before the output signal for a stand-alone resonator is attenuated by 3dB.

In the laboratory, testing of charge-biased resonators was done via the procedure summarized in Fig. 10. Here, all electrodes surrounding the disk resonator are first grounded, then a dc bias voltage V_{charge} is applied to the electrode underneath the disk structure. Next, a probe tip biased to V_{charge} is gently touched to the side wall of the conductive disk structure, charging it to V_{charge}. Upon pulling the probe tip away from the disk, the charge remains on the structure for a time governed by its leakage rate, which from [24], has a time constant on the order of 40 minutes—plenty long enough to take several high resolution measurement sweeps. Upon charging the resonator, the printed circuit board on which the resonator die is mounted is then transferred from the probe station into the custom built vacuum chamber and hooked up to the electrical feedthroughs. Mixing measurement [21] then proceeds as usual, except that the local oscillator and RF signals must now be combined at the input, rather than added to the dc-bias port of previous renditions.

Using this procedure, Figure 11 presents the measured frequency characteristic for an 18 μm-radius 60 MHz nickel disk with no center stem support, suspended only by the nitride material in the electrode-to-resonator gap. As shown, the disk exhibits a measured Q of 54,507, which clearly exposes the enormous impact of the stem on nickel resonator Q, and suggests that the nickel material quality is on par with other popular micromachinable materials (e.g., polysilicon, polydiamond) from a Q perspective. In fact, to our knowledge, the vacuum frequency-Q product of 3.3×10^{12} attained by this particular nickel resonator is the highest yet seen for any micro-scale *metal* resonator in the VHF range.

The use of charge biasing in the last experiment is intriguing, but begs the question: How long before leakage currents discharge the effective charge-bias to the point of noticeable performance degradation? To answer this, Figure 12 presents a measured plot of resonant peak height versus time. As shown in the figure, leaky discharging of the resonant structure in vacuum attenuates the output signal by 3 dB after 30 minutes, which is plenty long enough to make measurements, and long enough to allow charge refreshing via a very simple, low-power circuit.

VI. CONCLUSIONS

Wine-glass nickel micromechanical disk resonators with nitride dielectric capacitive transducer gaps have been demonstrated with frequency-Q products as high as 3.3×10^{12},

Table II: Material Property Comparison: Nickel Versus Other Popular MEMS Structural Materials

Material	**Young's Modulus *E* (GPa)**	**Density ρ (kg/m^3)**	**Acoustic Velocity (m/s)**	**Deposition Temperature (^{o}C)**	**Electrical Conductivity ($10^7/\Omega$m)**
Polysilicon	150	2.33	8,024	588	0.001
Polydiamond	1,144	3.5	18,076	800	0.001
Silicon Carbide	415	3.12	11,500	800	0.00083
$PolySi_{0.35}Ge_{0.65}$	146	4.28	5,840	450	0.005
Nickel	195	8.9	4,678	50	1.43

which is the highest to date for any micro-scale *metal* resonator device in the VHF range. This result proves that the intrinsic *Q* limit of plated nickel thin-films is more than adequate for VHF filtering and oscillator applications, and on par with that of other popular micromachinable materials, including polysilicon. Table II summarizes the material properties of the nickel material used in this work and compares them to that of other popular MEMS materials. As shown, the acoustic velocity of this work's nickel is 4,678 m/s, which is 1.71X smaller than that of polysilicon. However, high frequency devices should still be achievable. For example, for 1GHz, the needed radii of polysilicon and nickel disk resonators operating in their second radial-contour modes are 7.2 μm and 4.2 μm, respectively, which are on the same order and both easily achievable with present-day lithographic technology. The above characteristics, combined with the only 50^{o}C plating temperature required for its deposition, makes nickel a very strong candidate for use in modular MEMS-transistor merging processes seeking to integrate MEMS over finished foundry transistors in a fully monolithic, post-transistor fashion.

Acknowledgment. This work was supported by an NSF ERC in Wireless Integrated Microsystems.

References.

[1] J. Wang, *et al.*, "1.51-GHz polydiamond micromechanical disk resonator with impedance mismatched isolating support," in *Proc. IEEE Int Micro Electro Mechanical Systems Conf.*, Maastricht, The Netherlands, Jan. 25-29, 2004, pp. 641-644.

[2] S.-S. Li, *et al.*, "Micromechanical hollow-disk ring resonators," in *Proc. IEEE Int. Micro Electro Mechanical Systems Conf.*, Maastricht, The Netherlands, Jan. 25-29, 2004, pp. 821-824.

[3] R. L. Kubena, *et al.*, "Next generation quartz oscillators and filters for VHF-UHF systems," in *Tech. Dig., Int. Microwave Symp.*, San Francisco, CA, June 11-16, 2006.

[4] S.-S. Li, *et al.*, "Self-switching vibrating micromechanical filter bank," in *Proc. FC/PTTI Symp.*, Vancouver, Canada, Aug. 29-31, 2005, pp. 135-141.

[5] C. T.-C. Nguyen, "RF MEMS in wireless architectures," in *Proc. Design Automation Conf.*, Anaheim, CA, June 13-17, 2005, pp. 416-420.

[6] C. T.-C. Nguyen, "MEMS for frequency control and timing," in *Proc. FC/PTTI Symp.*, Vancouver, Canada, Aug. 29-31, 2005, pp. 135-141.

[7] T. A. Core, *et al.*, "Fabrication technology for an integrated surface-micromachined sensor," *Solid State Technol*, vol. 36, pp. 39-47, Oct. 1993.

[8] J. H. Smith, *et al.*, "Embedded micromechanical devices for the monolithic integration of MEMS with CMOS," in *Tech. Dig., IEEE Int. Electron. Device Mtg.*, Washington D.C., Dec. 10-13 1995, pp. 609-612.

[9] R. N. Chandler, *et al.*, "Single wafer encapsulation of MEMS devices," *IEEE Trans. Advanced Packaging*, vol. 26, no. 3, pp. 227-232, Aug. 2003.

[10] M. W. Putty, *et al.*, "A micromachined vibrating ring gyroscope,"in *Proc. Solid-State Sensors and Actuators Workshop*, Hilton Head, SC, June , 1994, pp. 213–220.

[11] C. T.-C. Nguyen, *et al.*, "An integrated CMOS micromechanical resonator high-*Q* oscillator," *IEEE J. Solid-State Circuits.*, vol. 34, no. 4, pp. 440-455, Apr. 1999.

[12] A. E. Franke, *et al.*, "Polycrystalline silicon-germanium films for integrated microsystems," *J. Microelectromechan. Syst.*, vol. 12, no. 2, pp. 160-171, Apr. 2003.

[13] G. He, *et al.*, "A single-crystal silicon vibrating ring gyroscope," in *Proc. Int. IEEE Micro Electro Mechanical Systems Conf.*, Las Vegas, NV, Jan. 20-24, 2002, pp. 718-721.

[14] W.-T. Hsu, *et al.*, "In situ localized annealing for contamination resistance and enhanced stability in nickel micromechanical resonators," in *Tech. Dig., Int. Conf. on Solid-State Sensors and Actuators*, Sendai, Japan, June 7-10, 1999, pp. 932-935.

[15] M. A. Abdelmoneum, *et al.*, "Stemless wine-glass-mode disk micromechanical resonators," in *Proc. IEEE Int. Micro Electro Mechanical Systems Conf.*, Kyoto, Japan, Jan. 19-23, 2003, pp. 698-701.

[16] Y.-W. Lin, *et al.*, "Series-resonant VHF micromechanical resonator reference oscillators," *IEEE J. Solid-State Circuits.*, vol. 39, no. 12, pp. 2477-2491, Dec. 2004.

[17] W.-T. Hsu, *et al.*, "Geometric stress compensation for enhanced thermal stability in micromechanical resonators," in *Proc. IEEE Int. Ultrason. Symp.*, Sendai, Japan, vol. 1, Oct.5-8, 1998, pp. 945-948.

[18] H. Guckel, *et al.*, "Closed loop controlled, large throw, magnetic linear microactuator with 1000μm structural height," in *Proc. IEEE Int. Micro Electro Mechanical Systems Conf.*, Heidelberg, Germany, Jan. 25-29, 1998, pp. 414-418.

[19] M. J. Biercuk, *et al.*, "Low-temperature atomic-layer-deposition lift-off method for microelectronic and nanoelectronic applications," *Appl. Phys. Lett.*, vol. 83, no. 12, pp. 2405-2407, Sep. 2003.

[20] H. Nathanson, *et al.*, "The resonant gate transistor," *IEEE Trans. Electron Devices*, vol. ED-14, pp. 117-133, Mar. 1967.

[21] J. R. Clark, *et al.*, "High-Q UHF micromechanical radial-contour mode disk resonators," *J. Microelectromechan. Syst.*, vol. 14, no. 6, pp. 1298-1310, Dec. 2005.

[22] F. D. Bannon, III, *et al.*, "High-Q HF micromechanical filters," *IEEE J. Solid-State Circuits.*, vol. 35, no. 4, pp. 512-526, Apr. 2000.

[23] J. Wang, *et al.*, "1.156-GHz self-aligned vibrating micromechanical disk resonator," *IEEE Trans.Ultrason. Ferroelect. Freq. Contr.*, vol. 51, no. 12, pp. 1607-1628, Dec. 2004.

[24] S.-S. Li, *et al.*, "Charge-biased vibrating micromechanical resonators," in *Proc. IEEE Int. Ultrason. Symp., Rotterdam, The Netherlands*, vol. 3, Sept. 18-21, 2005, pp. 1596-1599.